

# Gradiently Sodiated Alucone as an Interfacial Stabilizing Strategy for Solid-State Na Metal Batteries

Shumin Zhang, Yang Zhao, Feipeng Zhao, Long Zhang, Changhong Wang, Xiaona Li, Jianwen Liang, Weihan Li, Qian Sun, Chuang Yu, Jing Luo, Kieran Doyle-Davis, Ruying Li, Tsun-Kong Sham,\* and Xueliang Sun\*

All-solid-state metal batteries (ASSMBs) are attracting much attention due to their cost effectiveness, enhanced safety, room-temperature performance and high theoretical specific capacity. However, the alkali metal anodes (such as Li and Na) are active enough to react with most solid-state electrolytes (SSEs), leading to detrimental reactions at the metal–SSE interface. In this work, a molecular layer deposition (MLD) alucone film is employed to stabilize the active Na anode/electrolyte interface in the ASSMBs, limiting the decomposition of the sulfide-based electrolytes ( $\text{Na}_3\text{SbS}_4$  and  $\text{Na}_3\text{PS}_4$ ) and Na dendrite growth. Such a strategy effectively improves the room-temperature full battery performance as well as cycling stability for over 475 h in Na–Na symmetric cells. The modified interface is further characterized by X-ray photoelectron spectroscopy (XPS) depth profiling, which provides spatially resolved evidence of the synergistic effect between the dendrite-suppressed sodiated alucone and the insulating unsodiated alucone. The coupled layers reinforce the protection of the Na metal/electrolyte interface. Therefore, alucone is identified as an effective and bifunctional coating material for the enhancement of the metal/electrolyte interfacial stability, paving the way for rapid development and wide application of high-energy ASSMBs.

safety as well as high energy and power density.<sup>[1]</sup> Among those, all-solid-state sodium (Na) metal batteries (ASSMBs) are particularly promising for the high natural abundance and low cost of sodium, as well as the comparative performance with that of the all-solid-state lithium metal batteries (ASSLMBs).<sup>[2]</sup> The essence of ASSMBs is to develop excellent solid-state electrolytes (SSEs), which not only possess a high ionic conductivity at room temperature (RT) but also show good compatibility with the Na anode and cathode materials.<sup>[3]</sup> In recent years, some SSEs have been reported to exhibit ionic conductivity as high as  $10^{-3}$  S  $\text{cm}^{-1}$ , such as  $\beta$ -alumina,<sup>[4]</sup> NASICONs, polymer-based electrolytes,<sup>[5]</sup> and sulfide-based electrolytes.<sup>[3b,c,6]</sup> Generally, the oxide-based SSEs (including both  $\beta$ -alumina and NASICONs) show unfavorable thermodynamic stability, rigid instinct and high grain boundary resistance, which severely limit their applications. For polymer-based

## 1. Introduction

With a high demand on advanced energy storage systems, all-solid-state metal batteries (ASSMBs) are believed to be an emerging and competitive candidate due to their enhanced

electrolytes, it is still challenging to obtain decent ionic conductivity at RT despite their flexibility and low interfacial contact resistance. In contrast, sulfide-based electrolytes are the most promising candidates and meet most of the criteria of solid-state electrolytes in high-performance ASSMBs. Compared with analogous oxides, the sulfide SSEs consist of highly polarizable S atoms, which can weaken the electrostatic interactions with Na ions, thus facilitating Na-ion migration and exhibiting considerable ionic conductivity at RT.<sup>[7]</sup> Furthermore, the intimate electrolyte/electrode contact can reduce the interfacial resistance, boosting the Na-ion mobility at the interface and enabling high-performance ASSMBs.<sup>[8]</sup>

However, the interfacial issues are the most serious challenges to hinder the development of sulfide-based ASSMBs, especially on the Na anode/SSE interface. One of the problems is that sodium metal can thermodynamically react with most sulfide SSEs to form a poor interface with the reduced products ( $\text{Na}_3\text{Sb}$ ,  $\text{Na}_2\text{S}$ ,  $\text{Na}_2\text{Se}$ , and etc.),<sup>[9]</sup> continuously depleting both the SSE and Na metal. Meanwhile, the resultant large polarization can lead to high interfacial resistances and deterioration of battery performance. Another downside is that uneven Na deposition occurring at the Na/sulfide SSE interface is capable to cause the formation of Na dendrites, which penetrate along

S. Zhang, Dr. Y. Zhao, F. Zhao, Dr. C. Wang, Dr. X. Li, Dr. J. Liang, Dr. W. Li, Dr. Q. Sun, Dr. C. Yu, J. Luo, K. Doyle-Davis, R. Li, Prof. X. Sun  
Department of Mechanical and Materials Engineering  
University of Western Ontario  
London, Ontario N6A 5B9, Canada  
E-mail: xsun9@uwo.ca

S. Zhang, Dr. W. Li, Prof. T.-K. Sham  
Department of Chemistry  
University of Western Ontario  
London, Ontario N6A 5B7, Canada  
E-mail: tsham@uwo.ca

Dr. L. Zhang  
State Key Laboratory of Metastable Materials Science and Technology  
Yanshan University  
Qinhuangdao, Hebei 066004, P. R. China

 The ORCID identification number(s) for the author(s) of this article can be found under <https://doi.org/10.1002/adfm.202001118>.

DOI: 10.1002/adfm.202001118

the grain boundary of the SSE, resulting in short circuits of the batteries.<sup>[10]</sup> As such, the interfacial stability is the key to realize the high-performance sulfide-based ASSSMBs. Up to now, some effective approaches have been reported to address these issues. For example, Tian et al. reported a reactivity-driven hydrated interface showing the improved stability between Na<sub>3</sub>SbS<sub>4</sub> SSE and Na metal.<sup>[11]</sup> Nevertheless, the developments of ASSSMBs is still in its infancy, particularly interfacial studies.<sup>[11]</sup> Inspired from the ASSLMBs, interfacial engineering, including surface coatings and interlayer strategies, is the most facile and effective way to achieve a stable interface between the metal anode and SSE. Various coating and interlayer strategies (LiF-based functional interfaces,<sup>[12]</sup> organic polymer,<sup>[5]</sup> Al<sub>2</sub>O<sub>3</sub>,<sup>[13]</sup> and etc.) have been adopted to realize the integration of sulfide SSEs and Li anodes,<sup>[14]</sup> which can be applied to the Na counterparts and guide the research for ASSSMBs.

Herein, for the first time, we employ molecular layer deposition (MLD) technique in ASSSMBs to stabilize the Na anode/electrolyte interface. This is achieved by coating a 150-cycle alucone film on Na foil, alleviating the decomposition of sulfide-based electrolytes (Na<sub>3</sub>SbS<sub>4</sub> and Na<sub>3</sub>PS<sub>4</sub>) and suppressing Na dendrite growth. The protection mechanism of alucone is further investigated. Benefiting from an initial activation process, the pristine coating layer can be partly sodiated resulting in a sodiation gradient in the alucone which strengthens interfacial protection, thus enabling enhanced battery performance and cycling stability at RT. Due to the ability of stabilizing the Na metal/electrolyte interface in ASSSMBs, the MLD alucone deposition strategy presents enormous potential to be applied in high-energy-density ASSSMBs.

## 2. Results and Discussion

One remarkable advantage of sulfide-based SSEs is their softness, and this flexibility makes it possible to reversibly deform at the metal/SSE interface as the metal expands, maintaining performance during cycling.<sup>[15]</sup> However, these electrolytes are air sensitive enough to evolve gas during oxidation. Another intrinsic problem is that Na metal thermodynamically reacts with most thiophosphates to form poor ion-conducting products (e.g., Na<sub>2</sub>S).<sup>[9a]</sup> Even though substitution of the P can improve the electrochemical performance, those elements (As, Sb, and etc.) contributing to high ionic conductivity and chemical stability are redox-active, thus directly resulting in the decomposition of electrolytes in ASSSMBs (as shown in **Figure 1a**). Herein, we utilize alucone thin film deposited on Na foil to separate the Na metal and sulfide electrolytes. Typically, trimethylaluminum (TMA) and ethylene glycol (EG) are alternately sputtered on Na foil in a vacuum chamber at 85 °C, similar to our previous reports.<sup>[16]</sup> X-ray photoelectron spectroscopy (XPS) was carried out to study the surface composition of the 150-cycle alucone-coated Na sample, denoted as Na@mld150C. The XPS spectra show the existence of Al, C, and O. The peak positions of Al 2p and C 1s are in agreement with Al–O, C–H, and C–C references, confirming the successful deposition of MLD alucone (**Figure S1**, Supporting Information). To identify the appearance and depth information of that deposited layer, time-of-flight secondary ion mass spectrometry (ToF-SIMS) is

used to characterize the Na@mld150C anode. With the Cs<sup>+</sup> ion beam etching, the secondary ions, including C<sub>2</sub>Al<sup>-</sup> and AlO<sup>-</sup>, are removed and measured by the detector, while few Na<sup>-</sup> signals are detected, indicating that the Na surface is fully covered with alucone film (**Figure 1b**). Depth profiling records the intensity changes of secondary ions along with the sputtering time. The trends of these ions remain stable during the first 260 s whereas the curves of C<sub>2</sub>Al<sup>-</sup> and AlO<sup>-</sup> gradually decrease accompanied by the growth of Na<sup>-</sup> intensity (**Figure S2**, Supporting Information). Based on the sputtering rate (0.15 nm s<sup>-1</sup> on the Si substrate), the thickness of 150-cycle alucone layer could be estimated for over 50 nm, which is consistent with the growth rate of alucone.<sup>[16a]</sup> As shown in **Figure 1c**, ToF-SIMS 3D rendering models further demonstrate the elemental distribution of Na@mld150C according to the mass spectrometric data. For the *x*–*y* plane, the upper portion of the matrix models shows uniformly dispersed C<sub>2</sub>Al<sup>-</sup> and AlO<sup>-</sup>, which is attributed to the formation of a good coating layer on the Na foil. Due to the longitudinal distribution from alucone to Na and their close connection between each other, the signals of C<sub>2</sub>Al<sup>-</sup> and AlO<sup>-</sup> are gradually faded accompanied by the appearance of Na<sup>-</sup> along the *z* axis.

The effect of the above coating layer is evaluated by comparing the interfacial stability of Na (Na@alucone)/SSEs/Na (Na@alucone) symmetric cells. Two kinds of representative sulfide electrolytes, Na<sub>3</sub>SbS<sub>4</sub> and Na<sub>3</sub>PS<sub>4</sub>, are chosen because of their high ionic conductivities and relatively wide electrochemical stability windows. The synthesis procedures can be found in previous works.<sup>[3a,17]</sup> **Figure S3** (Supporting Information) shows the powder X-ray diffraction patterns (XRD) of the prepared Na<sub>3</sub>SbS<sub>4</sub> and Na<sub>3</sub>PS<sub>4</sub>, whose diffraction peaks are consistent with those of previously published Na<sub>3</sub>SbS<sub>4</sub> (t-Na<sub>3</sub>SbS<sub>4</sub>; ICSD no. 01-085-8198) and cubic Na<sub>3</sub>PS<sub>4</sub> (c-Na<sub>3</sub>PS<sub>4</sub>; mp-985584). Additionally, the room-temperature ionic conductivity is measured as 1.1 × 10<sup>-3</sup> and 8 × 10<sup>-5</sup> S cm<sup>-1</sup> for Na<sub>3</sub>SbS<sub>4</sub> and Na<sub>3</sub>PS<sub>4</sub> SSEs, respectively (**Figure S4**, Supporting Information). Even though Na<sub>3</sub>SbS<sub>4</sub> is an air-stable superionic conductor, calculated and experimental results show it has a higher reaction energy with Na metal compared to other solid electrolytes and the interfacial products lead to continuous decomposition of Na<sub>3</sub>SbS<sub>4</sub>.<sup>[18]</sup> Therefore, the chemical stability between Na<sub>3</sub>SbS<sub>4</sub> and (modified)-Na can be examined by observing the impedance evolution of symmetric cells at room temperature. The effect of alucone coatings with various thickness, such as 50-cycle alucone and 300-cycle alucone (denote as Na@mld50C and Na@mld300C, respectively), is also examined. Electrochemical impedance spectroscopy (EIS) was recorded every 4 h under open-circuit conditions. In **Figure S5a** (Supporting Information), Nyquist plots of EIS shows the growth of impedance from 620 to 1240 Ω during the first 24 h, suggesting that Na<sub>3</sub>SbS<sub>4</sub> and bare Na are highly unstable even through contact at open circuit. In sharp contrast, those Na foils coated with alucone exhibit good compatibility with Na<sub>3</sub>SbS<sub>4</sub>, which can be concluded from the negligible changes of total impedance in each group of Nyquist plots (**Figure S5b–d**, Supporting Information). Notably, the as-prepared Na@mld50C and Na@mld150C symmetric cells have little difference in overall resistance, whose initial impedance is 100 Ω, larger than that of as-prepared bare Na symmetric cell, indicating that alucone has

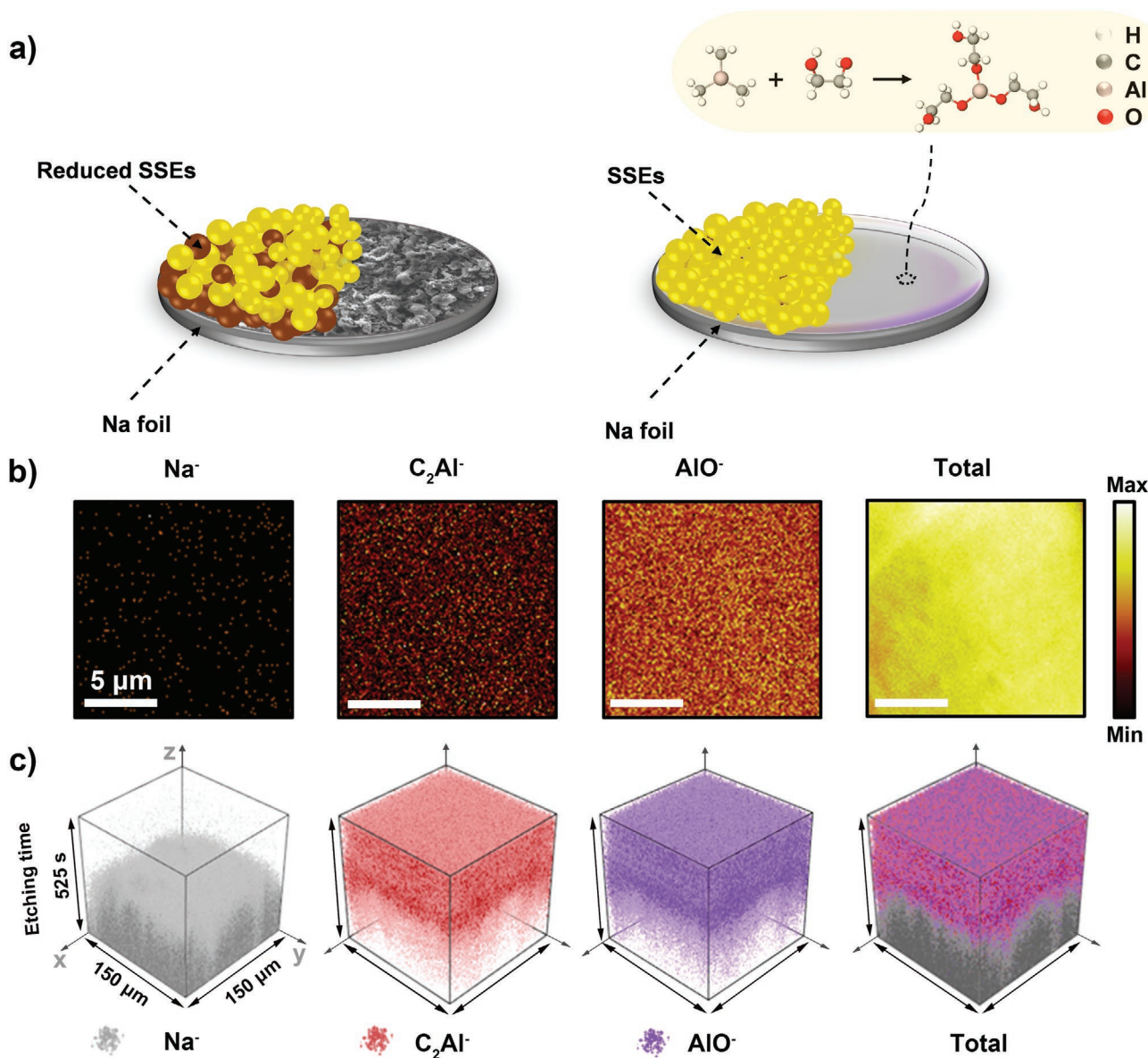


**Figure 1.** a) Schematic diagram of the reactive Na/sulfide-based SSEs interface and stable Na@alucone/sulfide-based SSEs interface. b) ToF-SIMS secondary ion images of Na@alucone anode before Cs<sup>+</sup> consecutive sputtering. c) 3D rendering models based on the depth scan of Na@mld150C anode by ToF-SIMS.

lower ionic conductivity. It should be mentioned that fresh alucone coating with 100 cycles is loosely packed and soft,<sup>[19]</sup> which is easily compressed between the solid anode and electrolyte during the battery assembly process, thus leading to a similar time-resolved EIS performance of Na@mld50C and Na@mld150C symmetric cells. However, too many MLD cycles produce a denser and thicker layer (Na@mld300C), causing an increased interfacial impedance of 1080 Ω. These results suggest that as-deposited thinner alucone coatings are insulating enough to restrain the interfacial reaction between Na and sulfide-based electrolytes, resulting from marginal increases to the initial interfacial impedance.

Next, the electrochemical stability of the Na–Na symmetric cells with and without MLD alucone assistance is investigated

at RT. After resting for 2 h, the cells were charged and discharged under a current density of 0.1 mA cm<sup>-2</sup> and a cutoff areal capacity of 0.1 mAh cm<sup>-2</sup>. As shown in **Figure 2**, the overpotential of Na plating/stripping in the bare Na symmetric cell dramatically increases from 56 mV to 1.2 V, which is caused by the detrimental side reactions between Na metal and Na<sub>3</sub>SbS<sub>4</sub>. Furthermore, there is a sudden drop of the potential after 269 h, which is a signal of cell short caused by Na dendrites. To optimize the thicknesses of the protective layers, the symmetric cells using Na@mld50C, 150C, and 300C were further investigated. From **Figure 2a**, the overpotential of the Na@mld50C symmetric cell grows slowly and levels off around 350 mV (vs Na<sup>+</sup>/Na) after a 160 h Na plating/stripping process. Corresponding with the above EIS data, this result also indicates that

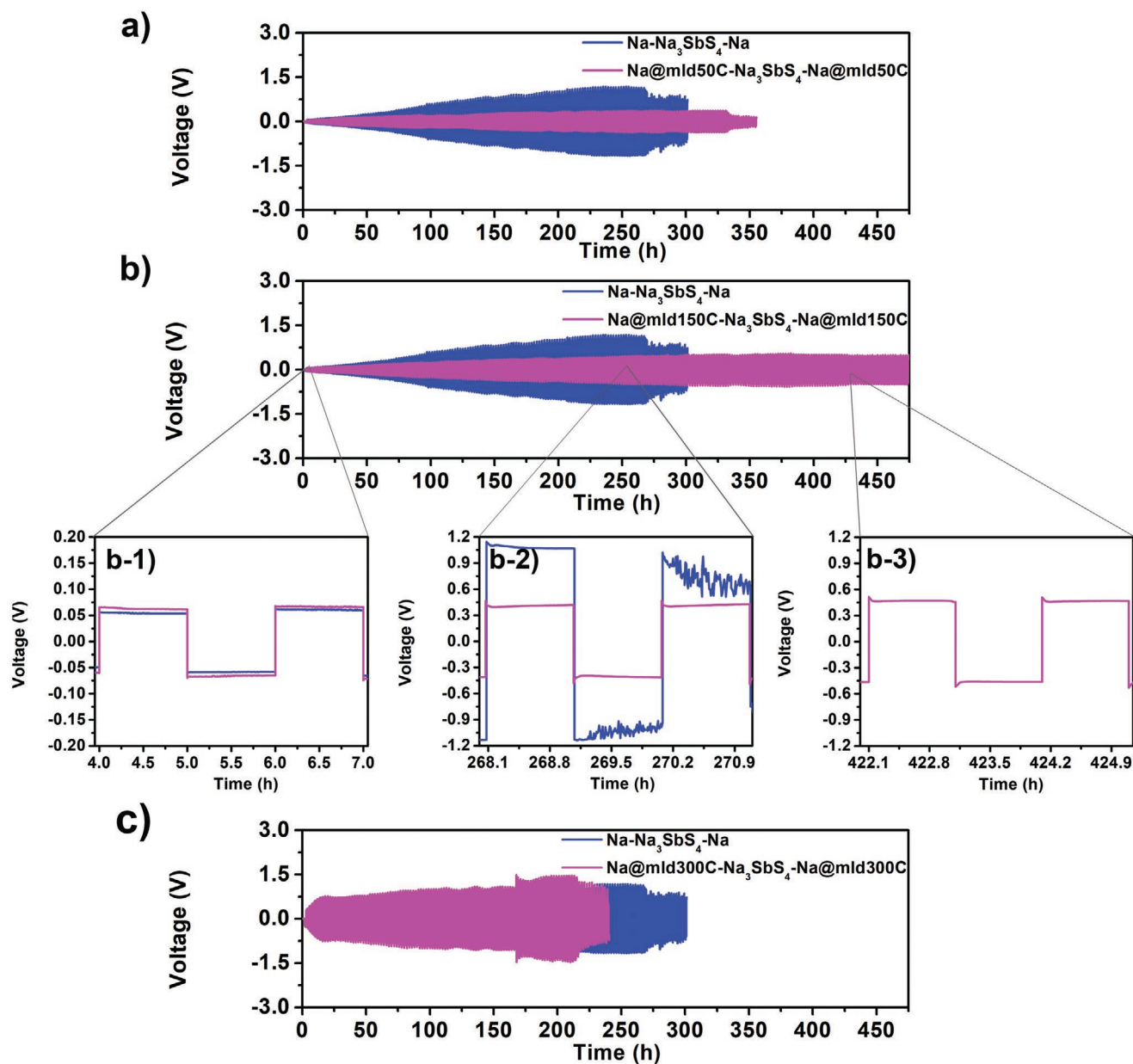


**Figure 2.** Comparison of Na plating/stripping behavior of Na symmetric cells at a current density of  $0.1 \text{ mA cm}^{-2}$  with an areal capacity of  $0.1 \text{ mAh cm}^{-2}$ : a) 50 cycles alucone (mld50C) versus bare Na. b) 150 cycles alucone (mld150C) versus bare Na. c) 300 cycles alucone (mld300C) versus bare Na.

alucone can effectively prevent the side reactions between Na and Na<sub>3</sub>SbS<sub>4</sub>, leading to improved interfacial stability. However, the cell survives only slightly longer, experiencing an internal short circuit after a 320 h cycling, indicating that 50 cycles of alucone are still insufficient to totally prevent Na dendrite penetration. Remarkably, the cell with 150-cycle alucone shows a small increase in polarization during the initial activation process and then stably cycles at around 450 mV for 475 h (Figure 2b). Compared with the Na@mld50C, compressed Na@mld150C is much compact to suppress the growth of Na dendrite, leading to outstandingly stable Na plating/stripping behavior. Its performance also surpasses other reported results with various Na sulfide SSEs (see the performance comparison

in Table S1, Supporting Information). However, increasing coating cycles from 150 to 300 gives rise a large overpotential at the beginning (see in Figure 2c), revealing that the thick and dense coating layer hinders Na<sup>+</sup> migration through the interface. Moreover, the same experiments conducted in the Na<sub>3</sub>PS<sub>4</sub> system (Figure S6, Supporting Information) with Na@mld150C symmetric cells also show the best performance. These results consistently demonstrate the effectiveness of alucone coating in suppressing the interfacial reactions between Na metal and sulfide-based SSEs as well as Na dendrite growth.

As alucone coating has been demonstrated to show a positive effect on the Na/SSEs interfacial issues, it is worth exploring how this protective layer works. Bare Na and Na@mld150C

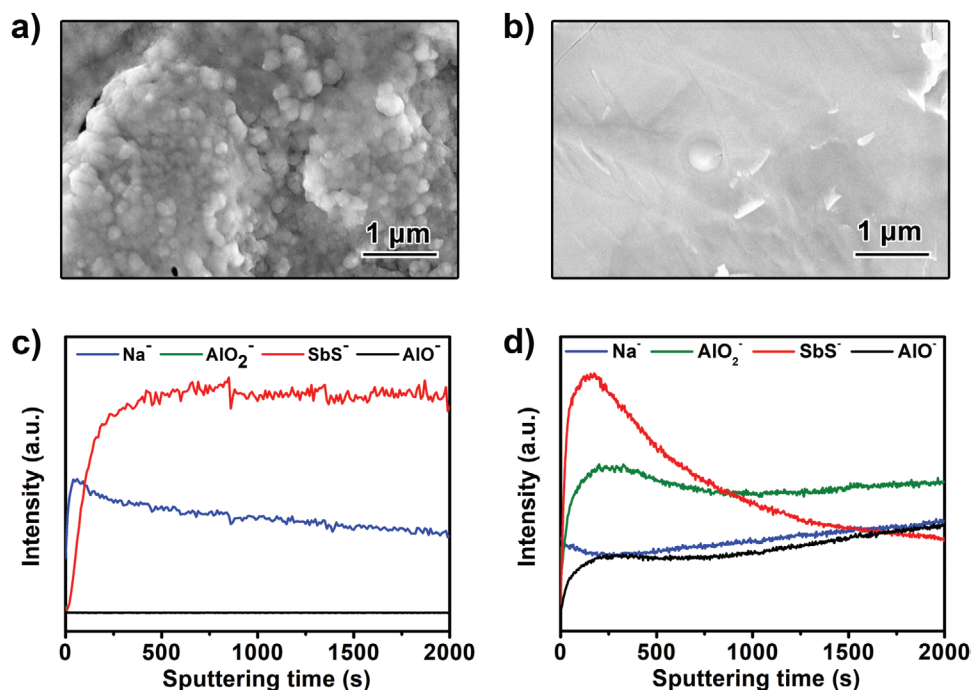


**Figure 3.** Top-side SEM images of the cycled Na|Na<sub>3</sub>SbS<sub>4</sub>|Na using a) bare Na and b) Na@mld150C electrodes; ToF-SIMS depth profiles of the cycled c) bare Na electrode and d) Na@mld150C electrode, respectively.

symmetric cells were disassembled after being cycled for 10 times. The interface between bare Na and Na<sub>3</sub>SbS<sub>4</sub> is rough with large black areas (as shown in Figure S7a, Supporting Information), indicating the formation of Na dendrites due to unstable interface of Na/Na<sub>3</sub>SbS<sub>4</sub>.<sup>[20]</sup> In comparison, the interface with alucone protection is much flatter and does not show any observable color changes after cycling (Figure S7b, Supporting Information). Then, the surface morphology of the above two buried-electrodes is investigated by scanning electron microscope (SEM). As shown in **Figure 3a**, in the absence of MLD coating, continuously protruding particles on the rough surface are observed for the bare Na metal electrode, indicating the growth of Na dendrites.<sup>[13]</sup> In contrast, the surface of Na@mld150C appears flat and smooth (Figure 3b), showing the evidence of restricting Na dendrite and providing intimate contact with Na<sub>3</sub>SbS<sub>4</sub> electrolyte. Alucone molecular layer are soft and flexible, thus such morphological differences are more capable to be caused by the sodiation of alucone forming a smooth and strong surface to reduce the Na dendrite. An analysis of the surface composition by energy-dispersive X-ray spectroscopy (EDS) reveals that the surface of Na@mld150C contains carbon, oxygen, sodium, aluminum, sulfur, and antimony, originating from both the electrolyte and coated electrode (Figure S8, Supporting Information). In order to deeply understand the nature of the cycled interface between Na and Na<sub>3</sub>SbS<sub>4</sub>, ToF-SIMS depth profiling is employed to analyze the specific chemical species as a function of time. With Cs<sup>+</sup> ions sputtering, the characteristic fragments for bare Na/Na<sub>3</sub>SbS<sub>4</sub> interface, including Na<sup>-</sup> and SbS<sup>-</sup>, are monitored (Figure 3c). The SbS<sup>-</sup> signal remains stable with fluctuations while Na<sup>-</sup> intensity decreases slowly after reaching an initial maximum. This trend difference suggests the decomposition of Na<sub>3</sub>SbS<sub>4</sub> during

the electrochemical cycling process. In Figure 3d, the signal intensity of SbS<sup>-</sup> dropped after first 180 s, indicating there were few electrolyte particles left on the cycled Na@mld150C surface. Notably, the alucone fragments (AlO<sub>2</sub><sup>-</sup> and AlO<sup>-</sup>) also had a maximum signal at the same sputtering period, but then showed a similar climbed trend with that of Na<sup>-</sup> species. Such in-depth variations in concentration are highly possible to attribute to the generation of two separate alucone-contained layers during Na plating/stripping.

As depicted above, the expected model of cycled Na@mld150C electrode can be divided roughly into top interlayer 1, interlayer 2 and Na foil at the bottom (**Figure 4a**). To further confirm this result and find out the chemical composition of each layer, XPS depth profiling is adopted to analyze chemical environments at the cycled electrolyte/metal interface. We totally collected 50 levels of elemental signals sputtering with an Al K $\alpha$  beam gun in an 8 h timeslot. Figure 4b shows the spectra of etching level 3. The presence of no reduced Na<sub>3</sub>SbS<sub>4</sub> electrolyte is evidenced by the Sb 3d spectra, which can be fitted as a Sb–S bond in the SbS<sub>4</sub><sup>3-</sup> tetrahedron.<sup>[20]</sup> Meanwhile, the peak positions of S 2p spectra (the S 2p<sub>3/2</sub> peaks at 163.3 and 161.5 eV and the respective S 2p<sub>1/2</sub> peaks at 164.5 and 162.7 eV) can be assigned to Sb=S and Sb–S–Na bonds, respectively.<sup>[20]</sup> At this etching level, the signals of Al and C are also detected, whose characteristic peaks are the same as that of as-prepared Na@mld150C anode. These results not only prove no decomposition of Na<sub>3</sub>SbS<sub>4</sub> at the Na<sub>3</sub>SbS<sub>4</sub>/Na@mld150C interface, but also support the existence of a Na<sub>3</sub>SbS<sub>4</sub>/alucone hybrid interlayer. As shown in Figure 4c,d, the overall evolution was summarized as representative Na and Al spectrum profiles (eight times signal collections after interval sputtering). Curves 1 and 2 at the top are assigned to interlayer 1 for the

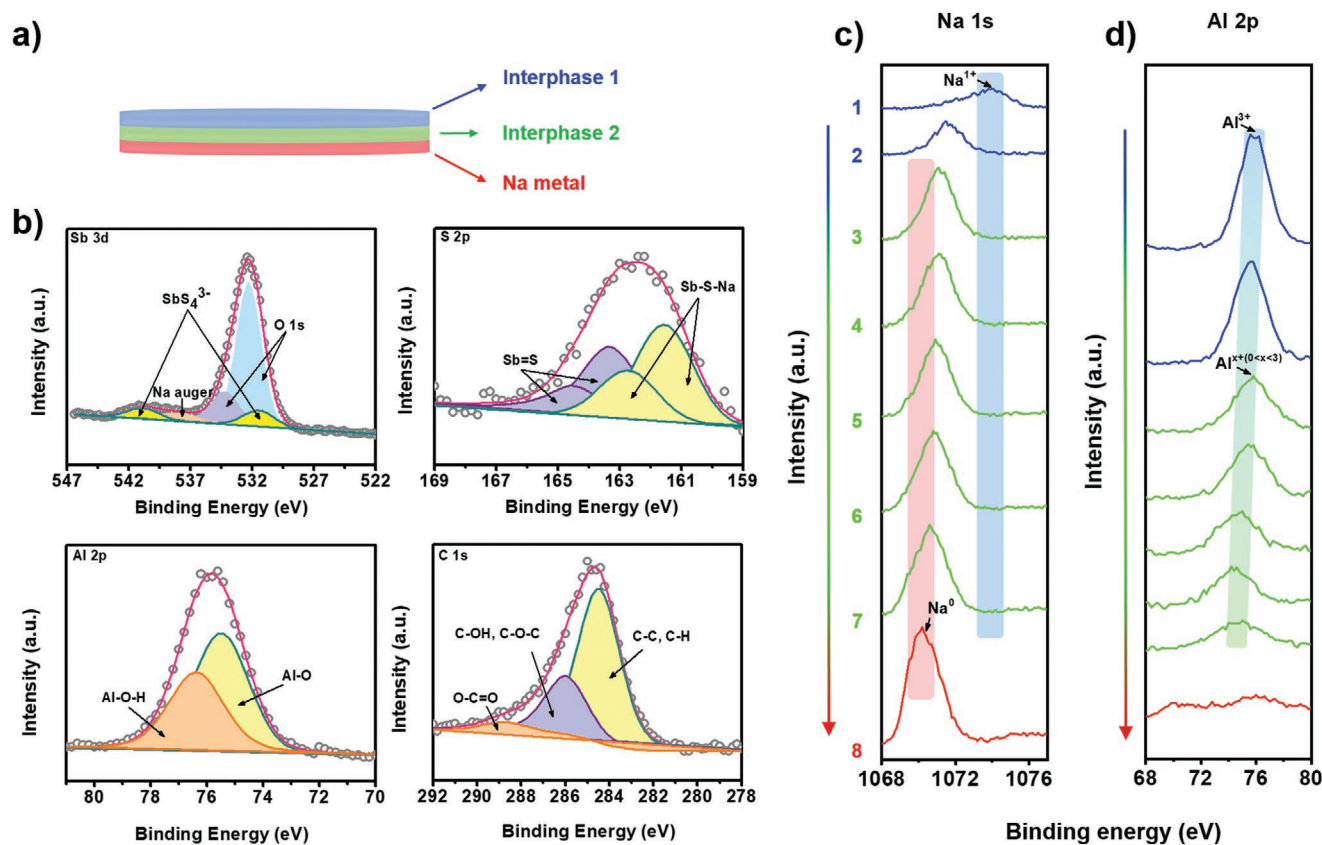


**Figure 4.** a) Presumed schematic diagram of Na@mlD150C/Na<sub>3</sub>SbS<sub>4</sub> interface after symmetric cell cycles. b) High-resolution XPS spectra of S 2p, Sb 3d, Al 2p and C 1s. The Sb 3d spectra indicate Sb<sup>5+</sup>. The peaks of Al 2p and C 1s represent the existence of alucone; XPS depth profiles of c) Na 1s and d) Al 2p d) of the cycled Na@mlD150C/Na<sub>3</sub>SbS<sub>4</sub> interface. The metallic Na (bottom curve) and interlayer 1 (top two curves) are identified in different sputtering depths, and the interlayer 2 is identified by the chemical valence changes of Na and Al.

Na 1s and Al 2p indicating Na<sup>+</sup> and Al<sup>3+</sup>, respectively, further proving the composition of interlayer 1 (Na<sub>3</sub>SbS<sub>4</sub> and alucone). It is worth noting that the peak positions of Al 2p shift to low energy from curve 3 to curve 7, suggesting that the sodiation of alucone forms Na–Al–C–O structure at a second interlayer (interlayer 2). For Na 1s curves (3–7, green color), the peaks at around 1070.4 eV are assigned to Na–O bond in Na–Al–C–O interlayer. Via a Na–O bond breaking/making process, the Na ion diffusivity can be accelerated.<sup>[21]</sup> During the formation of interlayer 2, the surface is gradually flattened for homogenous Na ion deposition, coinciding well with the above SEM images. Besides, the as-formed Na–Al–C–O structure is ductile and shows mechanical constraint to Na dendrites.<sup>[22]</sup> Finally, the intensity of Al 2p becomes weak and ultimately vanishes at the bottom level (Na foil layer), where the peak of Na 1s (indexed at 1070 eV) is assigned to metallic Na. The synergistic effect between dendrite-suppressed sodiated alucone and the insulating unsodiated alucone reinforces the protection of the Na metal/electrolyte interface, benefiting the electrochemical performance of ASSSMBs.

In order to demonstrate the potential application of the coated Na anode, we construct solid-state Na@mlD150C/Na<sub>3</sub>SbS<sub>4</sub>/TiS<sub>2</sub> ASSSMBs. The loading mass of the TiS<sub>2</sub> cathode is 8.92 mg cm<sup>-2</sup>. Figure 5a shows the cyclic voltammetry (CV) curves of this battery within the potential region of 1–2.8 V (vs Na/Na<sup>+</sup>) at

a scan rate of 0.1 mV s<sup>-1</sup>. During the first cycle, redox peaks at 1.85 and 2.4 V imply the reversible phase change between TiS<sub>2</sub> to Na<sub>x</sub>TiS<sub>2</sub>.<sup>[23]</sup> In the subsequent 2nd and 3rd cycles, highly overlapping CV curves indicate good cycling stability. Figure 5b depicts the galvanostatic charge/discharge profiles of Na@mlD150C/Na<sub>3</sub>SbS<sub>4</sub>/TiS<sub>2</sub> battery at a constant current density of 0.11 mA cm<sup>-2</sup>. Its discharge plateau at 1.85 V in the initial discharge curve shifts to 1.9 V in the second cycle onward, which is in accordance with the previously analyzed CV results. The discharge capacity initially reaches 200 mAh g<sup>-1</sup> and then reversibly maintains at 140 mAh g<sup>-1</sup> in the following cycles. A stable cycling at room temperature over 30 cycles and a high coulombic efficiency of ≈100% are demonstrated in Figure 5c, in sharp contrast to the performance when bare Na anode is used. The full cell performance with Na<sub>3</sub>PS<sub>4</sub> SSE is also tested, while the intrinsically poor ionic conductivity of Na<sub>3</sub>PS<sub>4</sub> leads to a large polarization and limited specific capacity. These results prove that the full cell addresses the interfacial instability issues and shows comparable performance with other reported sulfide-based ASSSMBs.<sup>[24]</sup>

### 3. Conclusion

In summary, for the first time, an MLD alucone-coated Na foil is successfully applied in ASSSMBs as this coating film

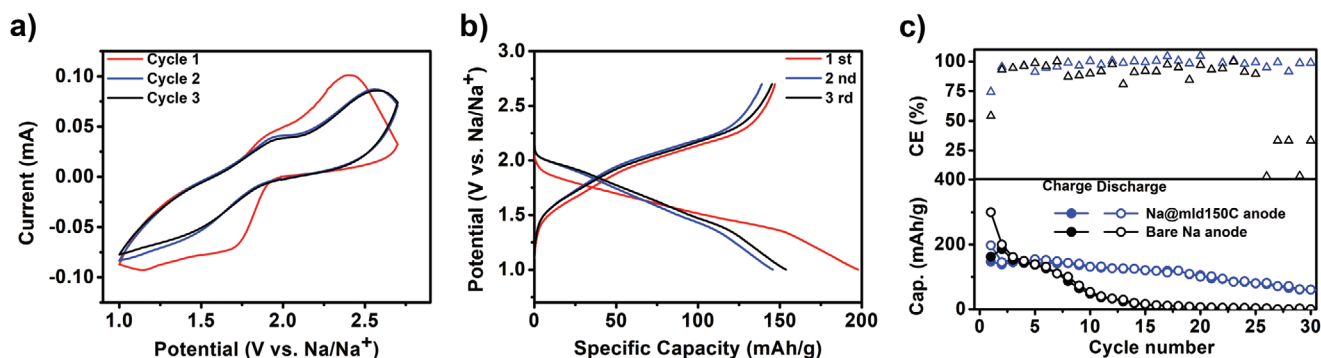


**Figure 5.** a) CV curves of all-solid-state Na@mld150C/Na<sub>3</sub>SbS<sub>4</sub>/TiS<sub>2</sub> battery. b) The charge and discharge profiles of Na@mld150C/Na<sub>3</sub>SbS<sub>4</sub>/TiS<sub>2</sub> cell performed at room temperature with a current density of 0.11 mA cm<sup>-2</sup>. c) cycling stability and coulombic efficiency of Na/Na<sub>3</sub>SbS<sub>4</sub>/TiS<sub>2</sub> and Na@mld150C/Na<sub>3</sub>SbS<sub>4</sub>/TiS<sub>2</sub> cells.

passivates the active metal anode, thus enabling a stable and long-life battery performance at room temperature. The optimized 150-cycle alucone coating layer can effectively stabilize the reactive Na<sub>3</sub>SbS<sub>4</sub> and Na metal interface, leading to enhanced room-temperature full battery performance as well as excellent cycling stability for over 475 h in Na–Na symmetric cells. Moreover, we use XPS depth profiling analysis to illustrate the protection mechanism of coating layer at the Na/sulfide-based SSEs interface: the insulating pristine alucone layer (Al–C–O) is partly sodiated upon electrochemical cycling, and this sodiated alucone (Na–Al–C–O) layer is beneficial for Na deposition as well as Na dendrite suppression. Such coupled interlayers synergistically stabilize the interface between Na metal and sulfide-based SSEs while suppressing dendrite growth, thus successfully realizing the ASSMBs with superb electrochemical performance. Our work identifies alucone as an effective and bi-functional coating material as its derivatives can stabilize the metal/electrolyte interface of solid-state batteries, paving the way for rapid development and wide utilization of high-energy ASSMBs.

## 4. Experimental Section

**Preparation of Na<sub>3</sub>SbS<sub>4</sub> Solid-State Electrolyte:** Na<sub>2</sub>S (Sigma Aldrich), Sb<sub>2</sub>S<sub>3</sub> (Sigma Aldrich, >99%) and Sulfur (Sigma Aldrich, 99.99%, trace metals basis) were purchased for using without further purification. An appropriate ratios of powder precursors (total 1 g) were sealed in zirconia ball milling pots in an Ar-filled glovebox. The mass ratio between the mixture and the zirconia ball is 1:40. After that, low-speed ball milling (150 rpm for 2 h) was firstly carried out to fully mix the starting materials, followed by a high-speed ball-milling process (510 rpm) for 20 h. Then, a certain amount of the ball-milled product was cold-pressed into pellet, and sealed in quartz tubes for annealing treatment. After heating at 550 °C for 5 h in the muffle furnace, the sample naturally cooled down to room temperature and was grinded to powder for further use.

**Preparation of Na<sub>3</sub>PS<sub>4</sub> Solid-State Electrolyte:** c-Na<sub>3</sub>PS<sub>4</sub> electrolyte was synthesized following the reported literature. Typically, a stoichiometric mixture of Na<sub>2</sub>S (Sigma Aldrich) and P<sub>2</sub>S<sub>5</sub> (Sigma Aldrich, >99%) were mechanochemical milled at 510 rpm for 1.5 h in Ar-filled zirconia ball milling pots, followed by a heat treatment at 270 °C for 2 h in Ar atmosphere. The products were then ground into fine powders for further use.

**Preparation of Alucone Film on Na Foils:** As the previously reported method from our group, molecular layer deposition (MLD) was used to prepare alucone coating layer on the fresh Na foils. Typically, fresh

Na foils with a diameter of 3/8 in. was prepared by pressing a piece of sodium (Sigma Aldrich, 99.9% trace metals basis) using a homemade press machine in an argon-filled glovebox. These fresh foils were then transferred into a Gemstar-8 ALD system without air exposure. Two precursors, trimethylaluminum (TMA) and ethylene glycol (EG), were alternatively deposited on the surface of Na foils at 85 °C to form alucone thin films. The MLD process used is as follows: 0.01 s/40 s/0.01 s/70 s TMA pulse/purge/EG pulse/purge. Different cycle numbers (50, 150, and 300) of alucone coating on Na foils are named as Na@mld50C, Na@mld150C and Na@mld300C, respectively.

**Ionic Conductivity Measurements:** Ionic conductivity of prepared Na<sub>3</sub>PS<sub>4</sub> and Na<sub>3</sub>SbS<sub>4</sub> electrolytes were measured by electrochemical impedance spectroscopy (EIS) and corresponding fitting. This was completed on a multichannel potentiostation 3/Z (German VMP3). The applied frequency range is 1 Hz–7 MHz and the amplitude is 20 mV. The test cell was fabricated as follows: 80 mg of the electrolyte was pressed into a pellet (diameter 1 cm, thickness 0.7 mm) with a pressure of ≈300 MPa. Successively, two pieces of indium (In) foil serving as the current collector were pressed on both sides of the electrolyte pellet in a model cell. To gain the Arrhenius plot, variable-temperature EIS was measured from –15 to 35 °C with an interval of 10 °C.

**Na/Na<sub>3</sub>SbS<sub>4</sub> (Na<sub>3</sub>PS<sub>4</sub>)/Na Symmetric Cells Assembly and Electrochemical Measurements:** 80 mg of electrolyte (Na<sub>3</sub>SbS<sub>4</sub> or Na<sub>3</sub>PS<sub>4</sub>) was pressed by ≈300 MPa to form solid pellet. Two pieces of Na foil were placed onto both sides of the electrolyte pellet and then pressed. The alucone-coated Na symmetric cells were assembled in the same way. Na plating/stripping experiments were carried out on LAND battery testing stations (CT-2001A, Wuhan Rambo Testing Equipment Co., Ltd.). Current density and cut-off capacity were set at 0.1 mA cm<sup>-2</sup> and 0.1 mAh cm<sup>-2</sup>.

**Na@mld150C/Na<sub>3</sub>SbS<sub>4</sub>/TiS<sub>2</sub> ASSMBs:** Using Na<sub>3</sub>SbS<sub>4</sub> as the electrolyte, prepared Na<sub>3</sub>SbS<sub>4</sub>/TiS<sub>2</sub> as the cathode composite, Na@mld150C as anode. 120 mg of the Na<sub>3</sub>SbS<sub>4</sub> electrolyte was pressed under ≈300 MPa to form a solid pellet (10 mm of diameter). 10 mg of Na<sub>3</sub>SbS<sub>4</sub>/TiS<sub>2</sub> powder was uniformly spread onto one side of Na<sub>3</sub>SbS<sub>4</sub> pellet and pressed under ≈360 MPa for 5 min. Finally, Na@mld150C foil was attached on the other surface of Na<sub>3</sub>SbS<sub>4</sub> pellet and pressed gently. The as prepared cell was sandwiched between two stainless-steel rods as current collectors and sealed in the model cell. Galvanostatic charge-discharge was conducted on the LAND battery test system. The voltage window was set as 1.0–2.8 V (vs Na/Na<sup>+</sup>). All cell fabrication processes were conducted in an Ar-filled glove box.

**Characterization Methods:** Scanning electron microscope (SEM) images and element mapping were obtained by using a Hitachi S-4800 field-emission scanning electron microscope (FE-SEM), acceleration voltage 5 kV) equipped with energy dispersive spectroscopy (EDS). X-ray diffraction (XRD) measurements were performed on Bruker AXS

D8 Advance with Cu K $\alpha$  radiation ( $\lambda = 1.54178 \text{ \AA}$ ). Capton tape was covered on the XRD holder to prevent from the air exposure. X-ray photoelectron spectroscopy (XPS) spectra were obtained by using Kratos AXIS Ultra Spectrometer system using a monochromatic Al K $\alpha$  X-ray source (3 kV, high current). The Kratos charge neutralizer system was used for all analyses. High resolution analyses were carried out with an analysis area of 200  $\mu\text{m}$  and a pass energy of 100 eV. The energy step size is 0.2 eV. For depth profiling, the same beam gun with a raster of 1 mm was used. These conditions have a calculated sputter rate of  $\approx 1.94 \text{ nm s}^{-1}$  based on Ta<sub>2</sub>O<sub>5</sub>. Multiple signal collections (50 times in total) were conducted after sputtering for 30 min at intervals. Time-of-flight (ToF-SIMS) measurements were conducted using an ION-TOF (GmbH, Germany) ToF-SIMS IV with a bismuth liquid metal ion source at Surface Science Western. The base pressure of the analysis chamber was  $\approx 10^{-8}$  mbar. The action of the primary ion beam bombardment on the sample surface induces the emission of negative secondary ions. Sputtering with a Cs<sup>+</sup> ion beam (3 keV) was used for depth profiling analysis.

## Supporting Information

Supporting Information is available from the Wiley Online Library or from the author.

## Acknowledgements

S.Z. and Y.Z. contributed equally to this work. This research was supported by the Natural Sciences and Engineering Research Council of Canada (NSERC), the Canada Research Chair Program (CRC), the Canada Foundation for Innovation, Ontario Research Fund (ORF), China Automotive Battery Research Institute Co., Ltd., Glatbat Solid-State Battery Inc., and the University of Western Ontario (UWO). Y.Z. appreciated the funding support of Mitac Elevate Postdoctoral Fellowship.

## Conflict of Interest

The authors declare no conflict of interest.

## Keywords

all-solid-state metal batteries, alucone-based bi-protective interface, molecular layer deposition, Na/electrolyte interface engineering

Received: February 6, 2020

Revised: March 6, 2020

Published online:

- [1] a) X. G. Han, Y. H. Gong, K. Fu, X. F. He, G. T. Hitz, J. Q. Dai, A. Pearce, B. Y. Liu, H. Wang, G. Rublo, Y. F. Mo, V. Thangadurai, E. D. Wachsman, L. B. Hu, *Nat. Mater.* **2017**, *16*, 572; b) K. K. Fu, Y. H. Gong, B. Y. Liu, Y. Z. Zhu, S. M. Xu, Y. G. Yao, W. Luo, C. W. Wang, S. D. Lacey, J. Q. Dai, Y. N. Chen, Y. F. Mo, E. Wachsman, L. B. Hu, *Sci. Adv.* **2017**, *3*, e1601659; c) H. Lee, P. Oh, J. Kim, H. Cha, S. Chae, S. Lee, J. Cho, *Adv. Mater.* **2019**, *31*, 1900376; d) H. Li, D. Chao, B. Chen, X. Chen, C. Chuah, Y. Tang, Y. Jiao, M. Jaroniec, S. Z. Qiao, *J. Am. Chem. Soc.* **2020**, *142*, 2012.
- [2] a) R. Bouchet, S. Maria, R. Meziane, A. Aboulaich, L. Lienafa, J. P. Bonnet, T. N. T. Phan, D. Bertin, D. Gignes, D. Devaux, R. Denoyel, M. Armand, *Nat. Mater.* **2013**, *12*, 452; b) B. Lee, E. Paek, D. Mitlin, S. W. Lee, *Chem. Rev.* **2019**, *119*, 5416; c) J.-J. Kim, K. Yoon, I. Park, K. Kang, *Small Methods* **2017**, *1*, 1700219; d) C. Ye, Y. Jiao, D. Chao, T. Ling, J. Shan, B. Zhang, Q. Gu, K. Davey, H. Wang, S.-Z. Qiao, *Adv. Mater.* **2020**, 1907557, <https://doi.org/10.1002/adma.201907557>; e) C. Ye, D. Chao, J. Shan, H. Li, K. Davey, S. Z. Qiao, *Matter* **2020**, *2*, 323.
- [3] a) A. Banerjee, K. H. Park, J. W. Heo, Y. J. Nam, C. K. Moon, S. M. Oh, S. T. Hong, Y. S. Jung, *Angew. Chem.* **2016**, *128*, 9786; b) W. D. Richards, T. Tsujimura, L. J. Miara, Y. Wang, J. C. Kim, S. P. Ong, I. Uechi, N. Suzuki, G. Ceder, *Nat. Commun.* **2016**, *7*, 11009; c) H. Wang, Y. Chen, Z. D. Hood, G. Sahu, A. S. Pandian, J. K. Keum, K. An, C. Liang, *Angew. Chem., Int. Ed.* **2016**, *55*, 8551; d) L. Zhang, D. C. Zhang, K. Yang, X. L. Yan, L. M. Wang, J. L. Mi, B. Xu, Y. M. Li, *Adv. Sci.* **2016**, *3*, 1600089; e) Z. Zhang, E. Ramos, F. Lalere, A. Assoud, K. Kaup, P. Hartman, L. F. Nazar, *Energy Environ. Sci.* **2018**, *11*, 87; f) C. Zhao, L. Liu, X. Qi, Y. Lu, F. Wu, J. Zhao, Y. Yu, Y.-S. Hu, L. Chen, *Adv. Energy Mater.* **2018**, *8*, 1703012.
- [4] a) X. C. Lu, G. G. Xia, J. P. Lemmon, Z. G. Yang, *J. Power Sources* **2010**, *195*, 2431; b) Z. Y. Wen, Y. Y. Hu, X. W. Wu, J. D. Han, Z. H. Gu, *Adv. Funct. Mater.* **2013**, *23*, 1005.
- [5] Z. Q. Zhu, M. L. Hong, D. S. Guo, J. F. Shi, Z. L. Tao, J. Chen, *J. Am. Chem. Soc.* **2014**, *136*, 16461.
- [6] a) D. C. Zhang, X. T. Cao, D. Xu, N. Wang, C. Yu, W. T. Hu, X. L. Yan, J. L. Mi, B. Wen, L. M. Wang, L. Zhang, *Electrochim. Acta* **2018**, *259*, 100; b) F. Zhao, J. Liang, C. Yu, Q. Sun, X. Li, K. Adair, C. Wang, Y. Zhao, S. Zhang, W. Li, S. Deng, R. Li, Y. Huang, H. Huang, L. Zhang, S. Zhao, S. Lu, X. Sun, *Adv. Energy Mater.* **2020**, *10*, 1903422.
- [7] a) S. L. Shang, Z. X. Yu, Y. Wang, D. H. Wang, Z. K. Liu, *ACS Appl. Mater. Interfaces* **2017**, *9*, 16261; b) Y. Wang, W. D. Richards, S. H. Bo, L. J. Miara, G. Ceder, *Chem. Mater.* **2017**, *29*, 7475.
- [8] a) A. Hayashi, K. Noi, A. Sakuda, M. Tatsumisago, *Nat. Commun.* **2012**, *3*, 856; b) C. Zeng, F. X. Xie, X. F. Yang, M. Jaroniec, L. Zhang, S. Z. Qiao, *Angew. Chem., Int. Ed.* **2018**, *57*, 8540.
- [9] a) H. M. Tang, Z. Deng, Z. N. Lin, Z. B. Wang, I. H. Chu, C. Chen, Z. Y. Zhu, C. Zheng, S. P. Onets, *Chem. Mater.* **2018**, *30*, 163; b) Y. Tian, T. Shi, W. D. Richards, J. Li, J. C. Kim, S. H. Bo, G. Ceder, *Energy Environ. Sci.* **2017**, *10*, 1150.
- [10] Y. S. Hong, N. Li, H. S. Chen, P. Wang, W. L. Song, D. N. Fang, *Energy Storage Mater.* **2018**, *11*, 118.
- [11] Y. S. Tian, Y. Z. Sun, D. C. Hannah, Y. H. Xiao, H. Liu, K. W. Chapman, S. H. Bo, G. Ceder, *Joule* **2019**, *3*, 1037.
- [12] Y. Gao, D. W. Wang, Y. G. C. Li, Z. X. Yu, T. E. Mallouk, D. H. Wang, *Angew. Chem., Int. Ed.* **2018**, *57*, 13608.
- [13] Y. Zhao, K. R. Adair, X. L. Sun, *Energy Environ. Sci.* **2018**, *11*, 2673.
- [14] a) Z. Shen, W. Zhang, G. Zhu, Y. Huang, Q. Feng, Y. Lu, *Small Methods* **2020**, *4*, 1900592; b) C. Ye, Y. Jiao, H. Jin, A. D. Slattery, K. Davey, H. Wang, S. Z. Qiao, *Angew. Chem., Int. Ed.* **2018**, *57*, 16703.
- [15] Q. Zhang, D. X. Cao, Y. Ma, A. Natan, P. Aurora, H. L. Zhu, *Adv. Mater.* **2019**, *31*, 1901131.
- [16] a) Y. Zhao, L. V. Goncharova, Q. Zhang, P. Kaghazchi, Q. Sun, A. Lushington, B. Q. Wang, R. Y. Li, X. L. Sun, *Nano Lett.* **2017**, *17*, 5653; b) C. H. Wang, Y. Zhao, Q. Sun, X. Li, Y. L. Liu, J. W. Liang, X. N. Li, X. T. Lin, R. Y. Li, K. R. Adair, L. Zhang, R. Yang, S. G. Lu, X. L. Sun, *Nano Energy* **2018**, *53*, 168.
- [17] A. Hayashi, K. Noi, N. Tanibata, M. Nagao, M. Tatsumisago, *J. Power Sources* **2014**, *258*, 420.
- [18] E. A. Wu, C. S. Kompella, Z. Y. Zhu, J. Z. Lee, S. C. Lee, I. H. Chu, H. Nguyen, S. P. Ong, A. Banerjee, Y. S. Meng, *ACS Appl. Mater. Interfaces* **2018**, *10*, 10076.
- [19] Y. Zhao, X. L. Sun, *ACS Energy Lett.* **2018**, *3*, 899.
- [20] P. Hu, Y. Zhang, X. W. Chi, K. K. Rao, F. Hao, H. Dong, F. M. Guo, Y. Ren, L. C. Grabow, Y. Yao, *ACS Appl. Mater. Interfaces* **2019**, *11*, 9672.

- [21] S. C. Jung, H. J. Kim, J. W. Choi, Y. K. Han, *Nano Lett.* **2014**, *14*, 6559.
- [22] X. G. Han, Y. Liu, Z. Jia, Y. C. Chen, J. Y. Wan, N. Weadock, K. J. Gaskell, T. Li, L. B. Hu, *Nano Lett.* **2014**, *14*, 139.
- [23] Y. P. Liu, H. T. Wang, L. Cheng, N. Han, F. P. Zhao, P. R. Li, C. H. Jin, Y. G. Li, *Nano Energy* **2016**, *20*, 168.
- [24] a) X. Y. Feng, P. H. Chien, Z. Y. Zhu, I. H. Chu, P. B. Wang, M. Immediato-Scuotto, H. Arabzadeh, S. P. Ong, Y. Y. Hu, *Adv. Funct. Mater.* **2019**, *29*, 1807951; b) I. H. Chu, C. S. Kompella, H. Nguyen, Z. Y. Zhu, S. Hy, Z. Deng, Y. S. Meng, S. P. Ong, *Sci. Rep.* **2016**, *6*, 33733.